ACS APPLIED MATERIALS & INTERFACES

Research Article

www.acsami.org

Effect of Local and Global Structural Order on the Performance of Perylene Diimide Excimeric Solar Cells

Tengling Ye,[†] Ranbir Singh,[†] Hans-Jürgen Butt,[‡] George Floudas,[§] and Panagiotis E. Keivanidis*,[†]

[†]Centre for Nanoscience and Technology@ PoliMi, Fondazione Istituto Italiano di Technologia, Via Pascoli 70/3/, 20133 Milano, Italy

[‡]Max Planck Institute for Polymer Research, Ackermannweg 10, D-55128 Mainz, Germany

[§]Department of Physics, University of Ioannina, 451 10 Ioannina, Greece

Supporting Information

ABSTRACT: Herein, we present a detailed study of the structure–function relationship in the organic photovoltaic (OPV) blend film composed of *N*,*N*′-bis(1-ethylpropyl)-perylene-3,4,9,10-tetracarboxylic diimide (EP-PDI) and the low energy gap copolymer of poly[4,8-bis-substituted-benzo[1,2-b:4,5-b′]dithiophene-2,6-diyl-*alt*-4-substituted-thieno[3,4-b]thiophene-2,6-diyl] (PBDTTT-E-O). The hierarchical organization in the photoactive layers and in extruded fibers of PBDTTT-E-O:EP-PDI was studied by fluorescence optical microscopy, atomic force microscopy, and wide-angle X-ray scattering (WAXS). WAXS revealed a nanophase-separated structure where PBDTTT-E-O domains of 4.3 nm in size coexist with EP-PDI domains of 20 nm size. Thermal annealing results in an increase of the PBDTTT-E-O domains, but it does not affect the size of the EP-PDI domains. Only the length of the EP-PDI columns in each domain is increased by thermal treatment. The photophysical characterization of the PBDTTT-E-O:EP-PDI layers and the electrical characterization of the corresponding OPV and unipolar carrier devices were performed. The quenching of the EP-PDI excimer luminescence is correlated with the photocurrent generation efficiency of the OPV devices. At high annealing temperatures the EP-PDI columnar length becomes larger than the previously reported diffusion length of the PDI excimer, and fewer excimers dissociate at the EP-PDI/polymer interfaces, leading to reduced photocurrent generation. The charge transport properties of the PBDTTT-E-O:EP-PDI blend film were studied as a function of the active layer microstructure that was tuned by thermal treatment. Thermal processing increases electron mobility, but the poor connectivity of the EP-PDI domains keeps hole mobility six times higher. In respect to the as-spun OPV device, a 3-fold increase is found in the power conversion efficiency of the device annealed at 100 °C. The high surface roughness of the PBDTTT-E-O:EP-PDI photoactive layer impedes the efficient extraction of charges, and a thin and smooth perylene-3,4,9,10-tetracarboxylic bisbenzimidazole overlayer is required for increasing the device performance to a power conversion efficiency (PCE) ∼ 1.7%. The inversion in the polarity of the device contacts resulted in an inverted device with PCE ∼ 1.9%. We provide rational guidelines for the accurate tuning of the layer microstructure in PDI-based photoactive layers of efficient OPV devices. Local disorder in the EP-PDI aggregates is essential (i) for the optimum electron transport that is ensured by the efficient connectivity of the EP-PDI columns in adjacent EP-PDI domains and (ii) for preventing the stabilization of the neutral photoexcitations in the EP-PDI domains in the form of slowly diffusive excimers. The high photocurrent generation efficiency achieved suggests the EP-PDI excimers are formed faster than the activation of triplet states, and photocurrent losses are minimized.

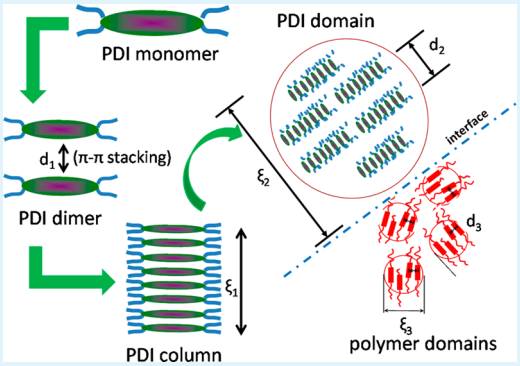

KEYWORDS: *perylene diimides, excimer, organic solar cells, nonfullerene acceptors, local and global structure, charge transport, extraction*

1. INTRODUCTION

Organic photovoltaic (OPV) devices are gaining increasing attention due to their high potential for achieving high power conversion efficiencies at low cost. Large-area OPV fabrication can be realized on mechanically robust and flexible substrates by utilizing low-cost deposition techniques that rely on high-throughput roll-to-roll production.[1,2] The central concept in OPV devices is the utilization of photoactive layers of bulk heterojunctions.[3,4] These are layers comprising polymeric electron donors mixed with fullerene derivatives that act as electron acceptors. Bulk heterojunction mixtures are soluble in most common organic solvents. Hence processing from solution gives rise to a bicontinuous network of polymer/fullerene phases. Exciton dissociation and charge photo-

Received: August 22, 2013
Accepted: October 28, 2013
Published: October 28, 2013

generation at the interfaces of these networks result in the formation of heteromolecular charge transfer states (hetero-CTs) with the hole residing in the polymer phase and the electron residing in the fullerene phase of the heterojunction. In photoactive layers of OPV devices the full dissociation of the hetero-CT states leads to the formation of charge-separated states (CS).[5] The produced mobile carriers are then available for extraction at the device electrodes to an external circuit. For the most optimized OPV devices today the efficient extraction of mobile carriers has led to power conversion efficiencies (PCEs) in the level of 10%.[6,7] Nonetheless, the commercialization of OPV-based modules is still limited by the high cost of produced watt-peak, partially due to the very high cost of the materials that are currently utilized in the photoactive layers of these devices.[8]

Despite their widespread use in OPV devices, fullerene-based acceptors absorb only weakly in the visible region. Therefore, they play a small role in solar light harvesting. Furthermore, the nontrivial synthesis of fullerene derivatives and their high price hinder widespread commercial accessibility. In this regard, other electron-acceptor molecules could potentially become useful in the field of OPV applications.[9−13] One class of electron-acceptor materials is the class of low-cost perylene dimide derivatives (PDIs).[14−22] PDIs are characterized by strong absorption in the visible region and relatively high electron mobility.[23] In addition, they can be synthesized in a scalable and economical way providing an alternative choice for n-type OPV materials.

Inherent to the design of optimal bulk heterojunctions is the control over the relevant donor/acceptor length scale and overall blend morphology. In the case of PDI-based OPVs there are three ways to adjust the morphology.[18] One way is by taking advantage of the inherent nanophase separation of block copolymers. The length scale of nanophases can be controlled at the synthesis level by suitable selection of the block molecular weights. Laju Bu and co-workers reported a PCE up to 1.50% under 1 Sun (AM1.5G) by means of synthesizing a monodisperse co-oligomer of PDI with electron donors.[24] Second, the molecular architecture of PDIs can be tuned. S. Rajaram and co-workers demonstrated that a nonplanar perylene, in combination with a hole-transporting polymer, can result in an average PCE value of 2.77% under 1.2 Sun (AM1.5G).[25] A third way is to vary the processing conditions and add suitable polymers or small molecules that exhibit compatibility with PDIs at a given length scale.[16,20] The latter methodology relies on a trial-and-error approach, and hitherto no rational guidelines have been established for gaining control over the PDI crystallization in OPV blend films.

PDIs are disk-shaped molecules that can form columnar aggregates.[26−28] When blended with polymeric matrices they have a tendency to crystallize, and this is one of the main reasons for the very low efficiencies obtained from PDI-based solar cells to date. Photocurrent losses result from the inefficient charge separation[29] of the electron−hole pairs that are produced after exciton dissociation at the PDI/polymer interface. Even when the production of mobile charges is efficient, electron transport is limited by structural defects and poor connectivity of the PDI domains.[30] Despite the detrimental role in the production of mobile carriers, the formation of PDI aggregates is expected to be essential for the macroscopic charge transport properties of organic photovoltaic layers.

Another important loss channel is the trapping of the initially photogenerated PDI excitons and the activation of homomolecular charge transfer states (homo-CTs) in the columnar PDI aggregate.[31,32] Homo-CTs are intermolecular excitations of PDIs, and they are formed by charge transfer reactions between a photoexcited PDI molecule and an adjacent ground-state PDI molecule.[27,33] A straightforward spectroscopic signature of the homo-CT state of PDI is the observation of the characteristic excimer-type PDI luminescence.[27,34,35] A broad photoluminescence (PL) band is detected at lower photon energy than the PL of the exciton state with a PL quantum yield (PLQY) lower than the PLQY of the exciton state and a prolonged lifetime.[36] Additionally, in respect to the exciton state, the homo-CT state of PDI has a shorter diffusion length.[37]

It seems unavoidable to achieve efficient PDI-based solar cells with photoactive layers free of homo-CT states that do not end up to emissive excimers at the expense of free charge photogeneration. A promising way of exploiting the absorbed photon energy without losing the appropriate PDI-based charge transport network is the utilization of the omnipresent PDI excimers in the production of photocurrent. The participation of the homo-CT states in the generation of hetero-CT states has been also suggested by recent experimental and theoretical studies in copper phthalocyanine/fullerene bilayers.[38]

The binding energy of the PDI excimer[39] can be overcome if appropriate PDI/polymer heterojunctions are formed that provide the necessary driving force for excimer dissociation. In a polymer/PDI blend, a large interfacial area between the PDI and polymer is a prerequisite for the efficient production of the hetero-CT states, and consequently the low diffusion length of the homo-CT state will limit their dissociation at the PDI/polymer interface. In this context a direct study of the PDI self-assembling properties as a function of the processing conditions of the OPV blend and the concomitant electrical performance of the corresponding device is still missing.

An understanding on the exact conditions that allow the formation of PDI networks without sacrificing the interfacial area between PDI and polymer is of paramount importance for the development of the next generation of PDI-based OPV devices. The identification of the structural motifs in the PDI-based OPV composites that result in high photocurrent generation efficiency is expected to be valuable feedback for the future synthesis of new PDI derivatives that could lead to the realization of efficient excimeric OPV devices. Recently, A. Sharenko et al. demonstrated an impressive PCE value of 3% under 1 Sun (AM1.5G), after the use of the diiodooctane (DIO) solvent additive in OPV blend films of the ethylpropyl-substituted perylene diimide derivative mixed with the low energy gap small molecular donor 7,7′-(4,4-bis(2-ethylhexyl)-4*H*-silolo[3,2-b:4,5-b′]dithiophene-2,6-diyl)bis(6-fluoro-4-(5′-hexyl-[2,2′-bithiophen]-5-yl)benzo[c][1,2,5]thiadiazole).[20] PCE values of 4.04% were achieved with a polymer:PDI system after combining the approach of S. Rajaram et al.[25] and of A. Sharenko et al.[40] Despite the rapid improvement in the performance of the PDI-based OPV devices, the exact role of the blend film microstructure in the processes of charge generation, transport, and collection remains unclear.

Herein we carefully study the correlation between the structural properties and the electrical performance of the efficient PDI-based composite of poly[4,8-bis-substituted-benzo[1,2-b:4,5-b′]dithiophene-2,6-diyl-*alt*-4-substituted-thieno[3,4b]thiophene-2,6-diyl] (PBDTTT-E-O) and the *N*,*N*′-bis(1-ethylpropyl)-perylene-3,4,9,10-tetracarboxylic dii-

mide (EP-PDI). Instead of directly focusing our efforts on receiving a high PCE value, we aim to unveil the physicochemical factors that can maximize the PCE of the PDI-based solar cell devices. The structural features of the PBDTTT-E-O:EP-PDI blend films are studied in the mesoscopic scale by atomic force microscopy (AFM) imaging. Further information on the structural properties of the polymer and EP-PDI components at the nanoscopic length scales is obtained by wide-angle X-ray diffraction on macroscopically oriented (extruded) fibers as a function of temperature. The detection of excimer-type EP-PDI luminescence in the time-integrated PL spectra of the blend films confirms the presence of emissive homo-CT states in the EP-PDI columns of the annealed films. The quenching of the EP-PDI excimer luminescence is correlated with the photocurrent generation efficiency of the OPV devices. The homo-CT state of EP-PDI is dominant in the thermally annealed photoactive layer, and its diffusion-limited arrival at the PDI/polymer interfaces prevents the efficient quenching of EP-PDI excimer luminescence. For the electrical characterization, a set of PBDTTT-E-O:EP-PDI solar cell devices with as-spun and thermally annealed photoactive layers are studied by means of external quantum efficiency spectra, $J-V$ photocurrent characteristics under simulated solar illumination, and photoexcitation-dependent photocurrent and charge transport measurements in unipolar devices. The power conversion efficiency (PCE) for the device annealed at 100 °C is ∼1.4%. At higher annealing temperatures the intracolumnar length of EP-PDI becomes larger than the previously reported diffusion length of the homo-CT state.[37] We discuss the importance that the structural order has for the excimer dissociation efficiency and for the charge transport properties of the PBDTTT-E-O:EP-PDI devices. The effect of surface roughness on the electron extraction efficiency at the contact between the electron-collecting electrode and the photoactive layer is addressed. Lastly, a PCE value of 1.9% is obtained when the PBDTTT-E-O:EP-PDI is incorporated in an inverted OPV device geometry.

2. MATERIALS AND METHODS

Materials. The chemical structures of PBDTTT-E-O and EP-PDI (both purchased from Solarmer Energy, Inc.) that were used in this study are shown in Figure 1. PBDTTT-E-O is a low bandgap polymeric donor, and the OPV devices based on its blends with a fullerene derivative exhibit PCEs greater than 5%.[41] EP-PDI is an electron acceptor that has been extensively studied in polymer-based photovoltaic and photodetector devices.[35,42]

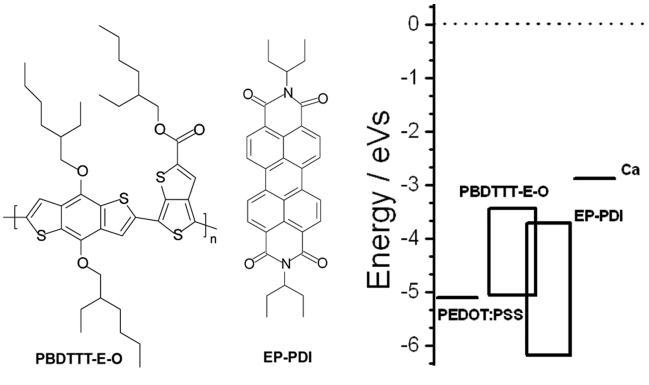

Figure 1. Chemical structures (left) of the materials used in this study and the energetic alignment (right) of their frontier orbitals with respect to the device electrodes PEDOT:PSS (hole collection) and Ca (electron collection).

Solar Cell Device Fabrication and Characterization. Non-inverted and inverted device geometries were prepared of the type glass/ITO/PEDOT:PSS/PBDTTT-E-O:EP-PDI/Ca/Al and glass/ITO/ZnO/PBDTTT-E-O:EP-PDI/V_2O_5/Ag, respectively. The glass/ITO substrates were precleaned with acetone, isopropanol, and a special detergent and dried under a flow of dry nitrogen. Before the deposition of the organic layers the ITO substrates were cleaned in O_2 plasma for 10 min. A PEDOT:PSS (Baytron P VP AI 4083, H.C. Stark) solution was then spin-coated at 6000 rpm onto the cleaned ITO substrates resulting in a thickness of approximately 30 nm. The PEDOT:PSS layer was annealed for 30 min at 140 °C in air. After that the devices were transferred into the glovebox. For preparation of the active layer PBDTTT-E-O was dissolved in chloroform at a concentration of 20 mg mL^{-1} and stirred overnight. Prior to deposition of the active layer the solution of PBDTTT-E-O:EP-PDI was filtered through a PTFE syringe filter. UV−vis spectroscopy confirmed that the filtering process did not affect the polymer:EP-PDI ratio in the deposited layers. The active layer was then spin-coated on top of the PEDOT:PSS film at 6000 rpm resulting in a film thickness of ∼105 nm. In all cases the film thickness of the organic layers was determined by a Dektak profilometer. Finally, calcium and aluminum electron-collecting electrodes were evaporated through a shadow mask on top of the active layer with a thickness of ∼10 and 100 nm. The films were post annealed at 100 °C for 15 min on a hot plate in the glovebox. Inverted OPV cells were prepared with the spin-coating deposition of an electron-selective ZnO layer[43] on the plasma-etched glass/ITO substrates. Following the deposition of the PBDTTT-E-O:EP-PDI photoactive layer, subsequent depositions of 2 nm thick V_2O_5 and 70 nm thick Ag layers were performed in vacuum (2×10^{-6} m bar) by thermal evaporation. For all devices, the active area of the pixels as defined by the overlap of anode and cathode area was 0.0525 cm^2. The photovoltaic performance was determined under simulated sunlight using an Oriel Sol3A Class AAA solar simulator. Mobility measurements were performed based on single carrier devices with photoactive layers prepared in an identical fashion to the OPV devices. The charge carrier mobility for each device was determined based on the space charge limited current method. Electron-only devices were prepared with electrodes of glass/ITO/ZnO and Ca/Al, whereas hole-only devices were prepared with electrodes of glass/ITO/PEDOT:PSS and Au. The electrical characterization of the fabricated solar cells was performed by means of external quantum efficiency (EQE) and by determining the basic photovoltaic parameters under simulated (AM1.5G) solar illumination. For preparing annealed devices the annealing step was performed with the use of a hot plate in a temperature between 40 and 200 °C after the deposition of the metal cathode for 15 min in the N_2-filled glovebox. The samples were then transferred onto a metallic cold surface for immediate cooling.

Wide-Angle X-ray Scattering (WAXS). A Rigaku RA-Micro 7 Desktop Rotating Anode X-ray generator was used with a maximum power of 800 W and brightness of 18 kW/mm^2 (operated at a tube voltage of 40 kV and a current of 10 mA) utilizing a Cu target. Osmic confocal optics were used for a monochromatic X-ray beam with 3 pinhole point collimation. The detection system was a MAR345 Image Plate Area Detector. The sample to detector distance was 31 cm. Samples were prepared as macroscopically oriented filaments with a diameter of 0.5 mm from a miniextruder at 75 °C. The WAXS measurements were made within the temperature range from 303 to 473 K on heating and on subsequent cooling in steps of 10 K. The recorded 2-D scattered intensities were investigated over the azimuthal angle and are presented as a function of the scattering wave vector q ($q = (4\pi/\lambda)\sin(2\theta/2)$, where 2θ is the scattering angle).

Time-Integrated Spectroscopic Characterization. Thin films of as-spun and annealed PBDTTT-E-O:EP-PDI were prepared in an identical fashion like for the case of the active layers of the solar cell devices. UV−vis absorption and photoluminescence spectra of the produced films were recorded with a UV-2700 Shimadzu spectrophotometer and a Horiba Jobin Yvon NanoLog spectrofluorimeter, respectively.

Light Intensity Dependent Short-Circuit Photocurrent. A diode pumped solid-state laser (DPGL2010F, Lambda Photometrics) was used for photoexciting the device at 532 nm, and the short-circuit device photocurrent was recorded with a Keithley electrometer (Source Meter Unit 2401). The laser output (10 mW, 1 mm diameter spot size) was attenuated with the use of neutral density filters of known transmittance values at the photoexcitation wavelength. For each device pixel several measurements were repeated for ensuring the stable response of the device photocurrent. All measurements were performed in ambient, and excellent reproducibility of the measured photocurrent was found. All measured devices were properly encapsulated with epoxy and glass.

Atomic Force Microscopy Imaging. Surface topography of all blend films was studied by atomic force microscopy (AFM) using an Agilent 5500 in tapping mode under ambient conditions. Topography and phase images were recorded simultaneously.

Fluorescence Optical Microscope Imaging (FOM). Reflected fluorescence optical microscopy images were obtained with a CCD camera (XC10) attached onto an Olympus polarizing optical microscope (BX51) operating in the reflection mode, after using a superwide band filter (U-MSWG2, 480−550 nm) for selectively using the spectral output of a Mercury lamp (U-LH100, 100 W) and integrating for 300 ms.

3. RESULTS

Figure 2a shows the UV−vis absorption spectrum of a PBDTTT-E-O:EP-PDI 30:70 (wt %) blend film. For comparison the UV−vis spectra of a pure PBDTTT-E-O film and a poly(styrene) (PS):EP-PDI 30:70 film are also shown.

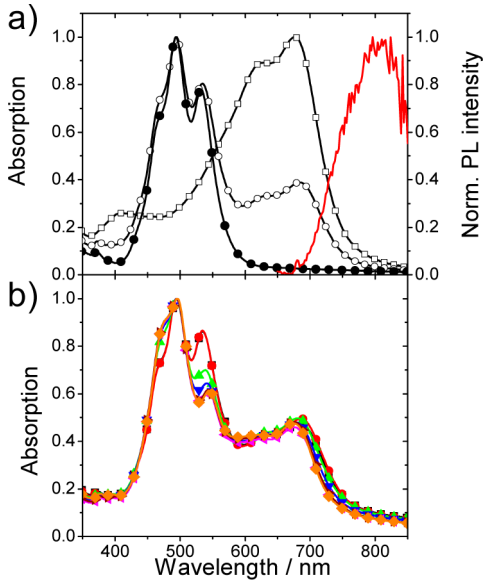

Figure 2. (a) Normalized UV−vis absorption spectra of a PBDTTT-E-O film (open squares) and of a PBDTTT-E-O:EP-PDI 30:70 blend film (open circles). For reference purposes the UV−vis spectrum of a control PS:EP-PDI film is also shown (filled circles). PL spectrum of a PBDTTT-E-O film on quartz substrate after photoexcitation at 620 nm (red line). (b) Normalized UV−vis absorption spectra of PBDTTT-E-O:EP-PDI blend films annealed at different temperatures: as-spun (squares) and annealed at 80 °C (circles), 100 °C (up triangles), 120 °C (down triangles), and 160 °C (diamonds).

The solid-state UV−vis spectrum of EP-PDI peaks at 495 nm, and it exhibits the typical features of a cofacial (H-type) aggregate of planar molecules in which molecular vibration is strongly coupled with the electronic transitions and a distribution of rotational displacements among the transition dipoles is found.[27] The main absorption band of PBDTTT-E-O is centered at lower photon energies with maximum absorption intensity at 680 nm. Since the absorption spectrum of PBDTTT-E-O is complementary to the absorption spectrum of EP-PDI, the UV−vis absorption spectrum of the blend spans from 420 to 800 nm; the PBDTTT-E-O:EP-PDI blend is an appropriate candidate system for the fabrication of the OPV layer with broad absorption in the visible range. In addition, the energy level matching between the frontier orbitals of the PBDTTT-E-O:EP-PDI bulk heterojunction confirms the suitability of this composite for charge photogeneration. According to Figure 1 the existing band offset is sufficient for driving an electron transfer from the polymer to PDI and a hole transfer in the reverse direction. For PBDTTT-E-O and EP-PDI the energy of the highest occupied molecular orbitals (HOMO) is −5.01 and −6.1 eV, respectively, whereas the energies of the lowest occupied molecular orbitals (LUMO) are −3.24 eV for PBDTTT-E-O and −3.8 eV for EP-PDI.[41,44]

Thermal annealing did not affect significantly the absorption properties of the PBDTTT-E-O:EP-PDI composite film. As shown in Figure 2b, thermal treatment results in a redistribution in the oscillator strength of the vibronics of the EP-PDI absorption band due to the changes in the contribution of the excitonic and homo-CT electronic components that dictate the EP-PDI absorption spectrum.[45,46]

Morphology and Surface Topography. Figure 3 presents a set of FOM images for PBDTTT-E-O:EP-PDI 30:70 blends after illumination with light in the wavelength range of 480−550 nm. For the case of the as-spun film no fluorescence could be detected indicating the intimate mixing of EP-PDI and PBDTTT-E-O that leads to complete

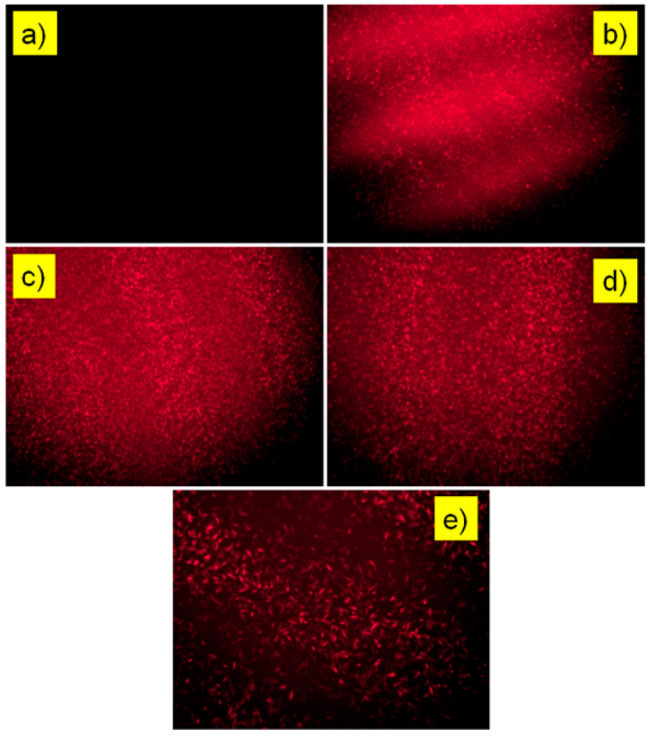

Figure 3. Fluorescence optical microscopy images of PBDTTT-E-O:EP-PDI 30:70 blends spun from chloroform on glass/ITO/PEDOT:PSS substrates and thermally annealed at different temperatures. The horizontal length of each micrograph image corresponds to 115 μm.

quenching of the EP-PDI excitations at the EP-PDI/PBDTTT-E-O interfaces. A similar effect was observed for the PBDTTT-E-O:EP-PDI film annealed at 40 °C (FOM images not shown), confirming that no phase separation between the polymer and EP-PDI components takes place on the micrometer length scale, prior to annealing at high temperatures. In contrast, the annealed films exhibit micrometer-sized features indicating phase-separated domains.

AFM imaging characterization of the PBDTTT-E-O:EP-PDI 70 wt % system was performed for a set of as-spun and annealed blend films. Low-resolution AFM images with scan lengths of 5 and 10 μm found that the root-mean-square (rms) surface roughness increases with thermal annealing; for the 5 μm scan the rms roughness increased from 20 nm for the as-spun film to 60 nm for the film annealed at 120 °C. Large aggregates were found to be the dominant objects in the layer surface with a lateral size virtually invariant to thermal treatment. Changes in the surface topography started to become resolved in AFM images that were acquired with scan length of 2 μm (see Figure S1 in Supporting Information). Higher-resolution AFM images with scan length of 500 nm were more informative (Figure 4a). The AFM images of the as-spun PBDTTT-E-O:EP-PDI 70 wt % blend films exhibited a relative uniform surface with a granular appearance. The individual granules had an extension of typically 25 nm. A similar structure was observed for blend films annealed at 40 °C (AFM images not shown). Thermal annealing above 40 °C led to a change in the layer morphology of the PBDTTT-E-O:EP-PDI blend films. When annealing at 80 and 100 °C slightly elongated features with sharp boundaries, 150 nm width and few hundred nanometer length were observed. When annealing at 120 °C the feature size decreased and became more rounded. PBDTTT-E-O films were prepared in an identical fashion, and their AFM images did not show these characteristic features (Figure 4b). Instead, they showed a granular structure for all annealing temperatures. The granules were larger when annealing at 80 and 100 °C than in the as-spun films and annealing at 120 °C. On the basis of previous studies on the morphology of PDI films,[15,35] it can be suggested that the appearance of the elongated features in the PBDTTT-E-O:EP-PDI blend films is related to the formation of PDI aggregates that are formed after the thermally induced coalescence of PDI in larger domains. The thermal treatment of the layers results in the demixing of the EP-PDI component from the PBDTTT-E-O matrix and in the increase of the EP-PDI cluster size. At small length scales (500 nm) the process of demixing is reflected on the size of the EP-PDI crystallites that is reduced in favor of the large EP-PDI cluster formation at the higher length scales (10 μm).

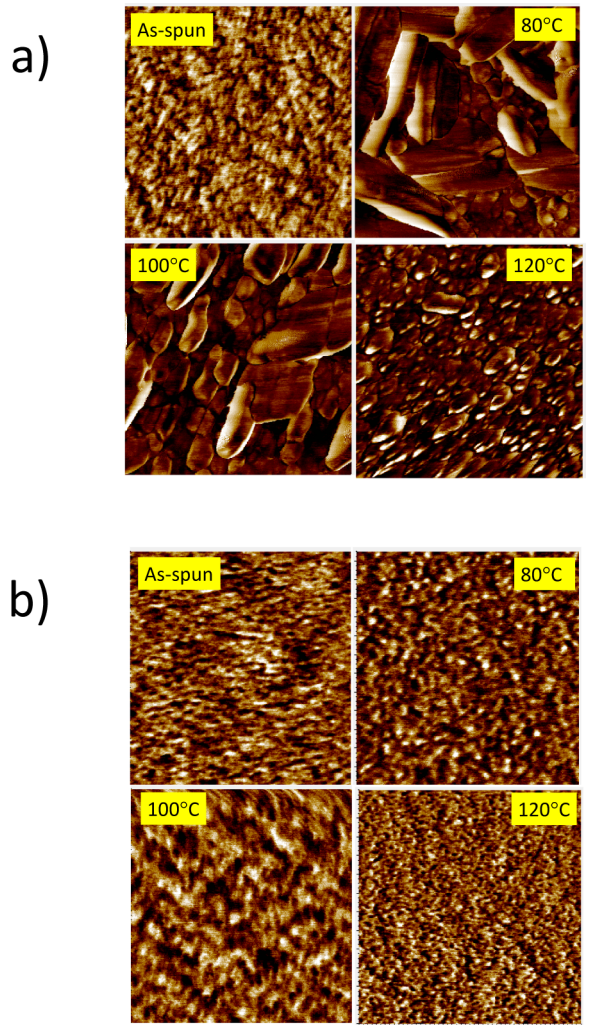

Figure 4. AFM phase images of (a) PBDTTT-E-O:EP-PDI 30:70 wt % films and (b) PBDTTT-E-O films spun from chloroform on glass/ITO/PEDOT:PSS substrates and thermally annealed at different temperatures. In all images the AFM window has a length of 500 nm.

Wide-Angle X-ray Scattering. The results from FOM and AFM revealed the demixing of the blend components and the growth of aggregated superstructures (beyond 1 μm) with increasing annealing temperature. On the other hand, the primary process of exciton diffusion and the microstructural features of the polymer/PDI interface have length scales of 10 nm, i.e., much below the resolution of optical microscopy and in the borderline of AFM imaging. To gain further insight into the microscopic structure of the PBDTTT-E-O:EP-PDI blend films we have employed WAXS. Figure 5 gives a schematic of the WAXS setup employed for the fibers and the scattered intensity from a series of images in a contour representation.

The different peaks contain reflections from the PBDTTT-E-O backbone and from stacked EP-PDI molecules in a columnar arrangement. The representative 2D image shown in the top panel of Figure 5 consists of both equatorial and meridional reflections. These reflections reveal that both the polymer backbones and the EP-PDI columnar axes are oriented along the fiber axis, i.e., perpendicularly to the X-ray beam. The contour plot of the wide-angle scattering X-ray intensities shown in the bottom panel of Figure 5 finds the first equatorial reflection around $q \sim 3.2$ nm^{-1}. This corresponds to the (100) reflection from the polymer backbone with backbone−backbone correlations of about $d \sim 1.95$ nm. This feature is very broad with a correlation length of ∼4.3 nm, suggesting weak backbone−backbone correlations at 30 °C (about three chain segments are correlated laterally). The peaks at higher wavevectors originate from EP-PDI. The main peak at $q \sim 3.9$ nm^{-1} suggests columnar stacking of EP-PDI with intercolumnar periodicity of ∼1.88 nm and a correlation length of ∼22 nm comprising laterally ∼12 columns. The latter gives the lateral length of coherence of EP-PDI columns and is also the length scale of nanophase separation. Equatorial reflections at higher q originate from the EP-PDI unit cell, whereas the meridional peaks reflect intracolumnar disk correlations at distances of ∼0.34 nm. Within the columns, EP-PDI disks are oriented

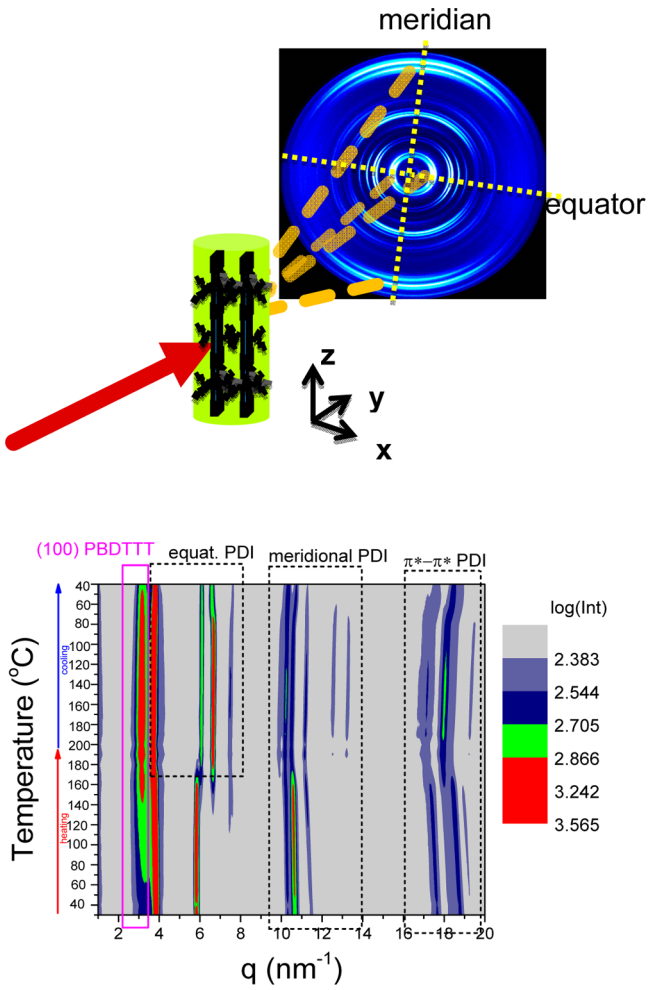

Figure 5. Top panel: WAXS geometry employed for fiber samples. The schematic shows the polymer chain organization within the fiber (backbones are oriented along the fiber axis). The EP-PDI columns (not shown) are also oriented along the fiber axis as evidenced by the meridional reflections. The 2-D image was taken after cooling to 30 °C following annealing at higher temperatures (~200 °C). Bottom panel: Contour (iso-intensity) plot of the wide-angle scattering X-ray intensities (in a log scale) from the PBDTTT-E-O:EP-PDI blend plotted as a function of the scattering wavevector for different temperatures obtained on heating and subsequent cooling. The (100) reflection corresponding to backbone–backbone correlations as well the equatorial and meridional EP-PDI reflections are shown.

perpendicularly to the columnar axis without any tilt. The elongated shape of the cores minimizes the π–π overlap and prevents molecules from tilting, in sharp contrast to more symmetric cores, such as in hexa-*peri*-hexabenzocoronenes that form a "herringbone" structure.[47] Therefore, these results at ambient temperature already suggest phase segregation and a higher organization (stacking) within the EP-PDI nanophase. The corresponding polymer and columnar periodicities as well as the interchain, intercolumnar, and intracolumnar correlation lengths are summarized in Table 1 at some temperatures.

Studying the scattering as a function of temperature is more informative with respect to the structural changes that may affect the polymer/EP-PDI interfaces and the domain size of the two blend components. As indicated in Table 1, increasing temperature improves backbone–backbone correlations, and this is more pronounced at the higher temperatures. For example, at 180 °C, the (100) reflection associated with the stacking of polymer backbones has a correlation length of ~8 nm; i.e., about five chain segments are correlated laterally. In addition, the improved polymer packing and increased order bring about a change in the EP-PDI equatorial reflections (at around 170 °C) associated with a slightly different unit cell. This suggests a more efficient nanophase separation between the polymer and EP-PDI stacks at the higher temperatures. Remarkably, the intracolumnar periodicity improves substantially on heating, from a value of 12 nm at 30 °C (each PDI column comprising about 36 disks) to about 19 nm at 180 °C (each PDI column comprising about 56 disks). On cooling, the high-temperature nanophase persists down to ambient temperature suggesting this as the equilibrium phase.

Overall the WAXS results from the oriented fibers revealed nanophase-separated polymer- and EP-PDI-rich domains with a characteristic length scale of phase separation in the order of 10–20 nm. However, most importantly they indicated improved backbone–backbone lateral correlations and much improved intracolumnar disk correlations. Both features can affect device performance. Improved polymer backbone correlations are known to have a positive impact on the device photocurrent generation.[48,49] Similarly, improved intracolumnar order and the concomitant annihilation of defects within the EP-PDI columns will improve the electron mobility within the columns.

These results on the morphology of the fibers can be representative for the morphology of the actual photoactive layer in devices. The large layer thickness in both cases precludes a sole preferential orientation (face-on vs edge-on orientation). Despite the preference of polymer backbones and EP-PDI columns to orient along the fiber axis, the molecular organization within the fiber cannot be considered as ideal (i.e., as in a single crystal). Thus, results on the self-organization measured either in thick films (~100 nm) or in fibers are expected to be comparable.

Photoluminescence Quenching. We have performed photoluminescence (PL) quenching measurements for

Table 1. Polymer Backbone and EP-PDI Columnar Characteristics As a Function of Temperature

temperature (°C)	interchain periodicity, $d_{backbone}$ (nm)	interchain correlation length, $\xi_{backbone}$ (nm)	intercolumnar periodicity, $d_{PDI\text{-}inter}$ (nm)	intercolumnar correlation length, $\xi_{PDI\text{-}inter}$ (nm)	intracolumnar periodicity, $d_{PDI\text{-}intra}$ (nm)	intracolumnar correlation length, $\xi_{PDI\text{-}intra}$ (nm)
30	1.95	4.3	1.88	22 ± 1	0.334	12 ± 0.5
60	1.97	4.6	1.89	20 ± 1	0.335	13 ± 0.5
90	1.98	4.9	1.89	20 ± 1	0.337	14 ± 0.5
120	1.98	5.2	1.90	21 ± 1	0.338	15 ± 0.5
140	1.98	5.7	1.91	23 ± 1	0.339	16 ± 0.5
160	2.00	6.5	1.92	23 ± 1	0.340	17 ± 0.5
180	2.02	7.5	1.94	21 ± 2	0.342	19 ± 1

PBDTTT-E-O:EP-EP-PDI 30:70 blend films as a function of annealing temperature in the range from ambient to 200 °C. For OPV composites, studying PL quenching is helpful in estimating the upper limit of generation yield of the hetero-CT states.[49] The high EP-PDI content in the blend and the weak absorption of the PBDTTT-E-O component in the spectral region of 500 nm allow the quasi-selective excitation of the EP-PDI component. Similarly, the vanishing absorption of the EP-PDI component in the spectral region of 600 nm allows selective excitation of the PBDTTT-E-O component. Control samples of pure PBDTTT-E-O films and PS:EP-PDI blend films were prepared and characterized in an identical fashion and were employed as references. Figure 6 presents the PL

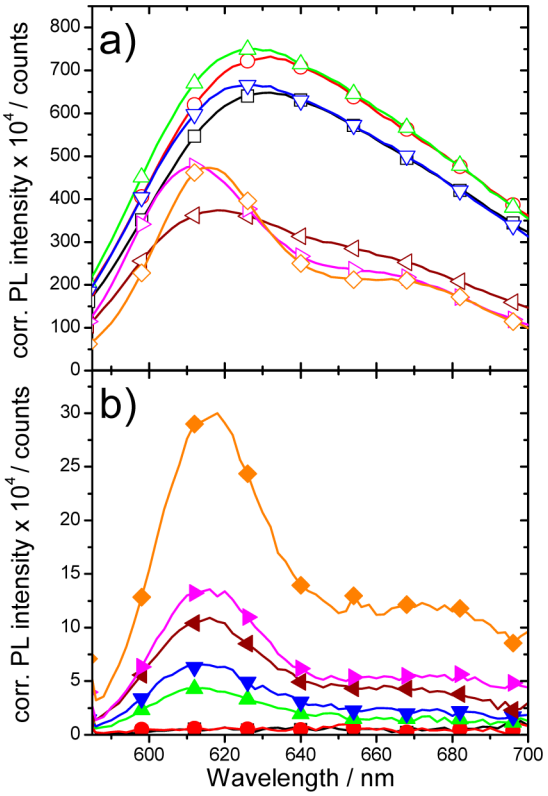

Figure 6. Photoluminescence spectra of as-spun and annealed (a) PS:EP-PDI films (open symbols) and (b) PBDTTT-E-O:EP-PDI (filled symbols). All films were deposited on quartz substrates and photoexcited at 530 nm: as-spun (squares), 40 °C (circles), 80 °C (up triangles), 90 °C (down triangles), 100 °C (right-tilt triangles), 120 °C (left-tilt triangles), 160 °C (diamonds.).

spectra of the PS:EP-PDI and the PBDTTT-E-O:EP-PDI blend films as a function of thermal annealing following photoexcitation of EP-PDI at 530 nm. The excimer-like luminescence of EP-PDI is detected in the spectral region of 620 nm. Following photoexcitation of the pure PBDTTT-E-O film at 620 nm, the PBDTTT-E-O luminescence was detected at 810 nm (Figure 2a).

For the PBDTTT-E-O:EP-PDI blend films excited at 620 nm, the PBDTTT-E-O luminescence was completely quenched. The vanishing spectral overlap between the emission spectrum of PBDTTT-E-O and the absorption spectrum of EP-PDI excludes the possibility that the observed PL quenching of the PBDTTT-E-O emission is a result of a resonant energy transfer between photoexcited polymer and ground-state EP-PDI. In contrast, energy transfer events cannot be neglected in the case where the EP-PDI component is photoexcited. The very high values of the spectral overlap between the EP-PDI excimeric emission and the UV–vis absorption of PBDTTT-E-O in the PBDTTT-E-O:EP-PDI 30:70 blend (see Figure S2 in Supporting Information) suggest that EP-PDI excimers could energy transfer to the polymer phase with a high efficiency.

On the basis of the spectra in Figure 6, we have determined the spectrally integrated PL intensity of the EP-PDI excimer luminescence (586–708 nm) in the two different matrices of PS and PBDTTT-E-O. Previous studies showed that the spectral integral of the EP-PDI emission in OPV composites is proportional to the PLQY of the composite.[35] With respect to the corresponding spectra of the control PS:EP-PDI sample, the quenching efficiency of the EP-PDI emission in the PBDTTT-E-O:EP-PDI films remains higher than 90% at all temperatures.

Thermal annealing reduces the EP-PDI PL quenching in the PBDTTT-E-O:EP-PDI 30:70 blend, and in the annealed films the recovery of the characteristic EP-PDI excimer luminescence at 620 nm is observed. In light of the structural changes within the EP-PDI columns as determined by WAXS, the observed reduction in the EP-PDI PL quenching efficiency can be assigned to the nanophase separation of the EP-PDI and PBDTTT-E-O domains. The overall quenching of the EP-PDI luminescence is a result of all deactivating excited-state pathways that can quench the EP-PDI excimer emission. The increased length of the EP-PDI columnar aggregates prevents the diffusion of the EP-PDI excimers at the EP-PDI/polymer interfaces, and it reduces the number of excimers that can charge transfer. In addition, the formation of larger size EP-PDI clusters after annealing negatively affects the efficiency of energy transfer from the EP-PDI excimer to the polymer phase due to the increased distance between EP-PDI and PBDTTT-E-O.

Solar Cell Characterization. We have characterized a set of photovoltaic devices based on the PBDTTT-E-O:EP-PDI blend films which were annealed at different temperatures. Devices of glass/ITO/PEDOT:PSS (30 nm)/PBDTTT-E-O:EP-PDI (105 nm)/Ca (10 nm)/Al (100 nm) were fabricated with photoactive layers unannealed and annealed between 40 and 200 °C. The device external quantum efficiency (EQE) was determined under monochromatic illumination, and their photocurrent density–voltage (J–V) characteristics were recorded under simulated solar light (0.93 Sun, AM1.5G).

Figure 7a presents the EQE curves, and Figure 7b presents the J–V curves of the devices annealed at different temperatures. The effect of thermal treatment positively affects device performance. The EQE spectra reveal that both PBDTTT-E-O and EP-PDI components contribute to an increase in the photocurrent for thermal annealing temperatures up to 100 °C. On the basis of the EQE spectra of the devices annealed at temperatures above 100 °C it is found that photon absorption by the EP-PDI phase (435–550 nm) delivers constant current, whereas photon absorption by the PBDTTT-E-O phase (590–800 nm) results in reduced photocurrent with respect to the device annealed at 100 °C (see also Figure S3 in the Supporting Information). As a net result the maximum photocurrent is obtained for the device with the PBDTTT-E-O:EP-PDI layer annealed at 100 °C. Similarly, the maximum PCE value under simulated solar light illumination is obtained at 100 °C, and it is three times higher than the PCE of the device with the as-spun photoactive layer. The positive effect of thermal annealing at 100 °C reflects the efficient separation of charges after the

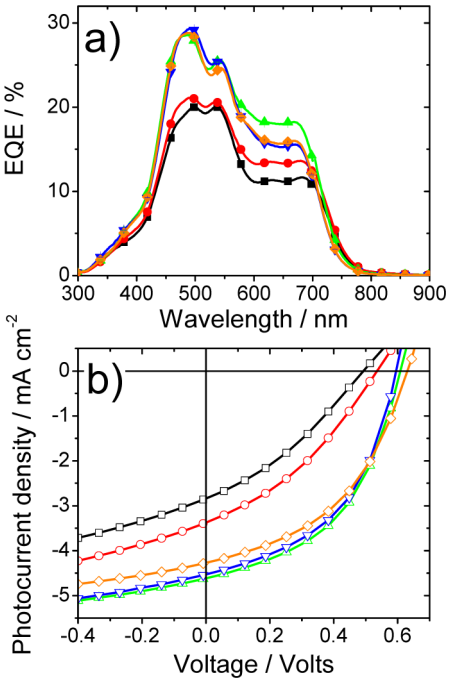

Figure 7. (a) Average external quantum efficiency curves (% EQE) of PBDTTT-E-O:EP-PDI devices annealed at different temperatures (filled symbols) and (b) photocurrent density versus voltage (J–V) curves of the best devices annealed at different temperatures (open symbols): as-spun (squares), 80 °C (circles), 100 °C (up triangles), 120 °C (down triangles), and 160 °C (diamonds).

dissociation of EP-PDI and PBDTTT-E-O excited states at the PBDTTT-E-O/EP-PDI interfaces. This is in agreement with the improved structural order[48,49] of both components at this annealing temperature. Since the EP-PDI component has the strongest absorption in the blend, it also has the dominant contribution in the generation of photocurrent. Table 2 summarizes the averaged and best values of the short-circuit photocurrent density (J_{sc}), open-circuit voltage (V_{oc}), fill factor (FF), and PCE parameters for these devices when measured under 0.93 Sun (AM1.5G). No improvement was found in the device metrics of the PBDTTT-E-O:EP-PDI system after the use of the DIO solvent additive in a set of devices with increased additive content, as previous studies have demonstrated for other PDI-based composites.[25,40]

Device Engineering. Next, we explored the effect on the PCE after depositing a thin and smooth PTCBI interlayer[50] on top of the as-spun PBDTTT-E-O:EP-PDI photoactive layer. The complete bilayer device was annealed at 100 °C. A range of overlayer thicknesses were tested (between 5 and 20 nm) deposited by thermal evaporation with a growth rate of 0.4 Å/s. The optimum device performance was obtained for the PTCBI layer of 7.5 nm; the PCE improved further to the value of 1.68% ± 0.06%.

Figure 8 presents the effect of the overlayer in the main device metrics of PBDTTT-E-O:EP-PDI. The differences in the open-circuit, $\Delta V_{oc} = V_{oc}(\text{PTCBI}) - V_{oc}$, and short-circuit photocurrent density, $\Delta J_{sc} = J_{sc}(\text{PTCBI}) - J_{sc}$, fill factor, ΔFF = FF(PTCBI) − FF, and power conversion efficiency, ΔPCE = PCE(PTCBI) − PCE, are plotted as a function of PCTBI overlayer thickness. Here V_{oc}(PTCBI), J_{sc}(PTCBI), FF(PTCBI), and PCE(PTCBI) correspond to the V_{oc}, J_{sc}, FF, and PCE of the PBDTTT-E-O:EP-PDI/PTCBI bilayer devices. Both single-layer and bilayer devices were characterized under 0.93 Sun (AM1.5G).

Comparison of the device metrics of the optimized devices made by PBDTTT-E-O:EP-PDI/PTCBI and PBDTTT-E-O:EP-PDI suggests the improvement of the FF parameter in the device with the PTCBI overlayer as the main factor that leads to the enhancement of PCE. The extraction of electrons at the interface of the photoactive layer and the electron-collecting electrode is one of the factors that limits the performance of the PBDTTT-E-O:EP-PDI devices. Up to a 10 nm thick PTCBI layer, charge extraction and collection are optimized. For thicker PTCBI layers the FF and V_{oc} were reduced indicating a poor electron transport. The surface topography of the PBDTTT-E:EP-PDI and PBDTTT-E:EP-PDI/PTCBI layers is shown in the Supporting Information (Figure S4).

We have studied the effect of the inverted OPV (i-OPV) device geometry on the performance of the PBDTTT-E-O:EP-PDI system. The structure of the i-OPV device was glass/ITO/ZnO/PBDTTT-E-O:EP-PDI/V_2O_5 (2 nm)/Ag. Figure 9 presents the device EQE under monochromatic illumination (Figure 9a) and the corresponding J–V curve under simulated solar light (Figure 9b, 0.83 Sun, AM1.5G) whereas the main device metrics are presented in Table 2. The PCE of the i-OPV device further increased to 1.9%. The V_{oc} parameter is increased, and slightly higher J_{sc} is obtained without a significant improvement in the FF value. In Figure 9c, the short-circuit photocurrent, I_{sc}, of the inverted PBDTTT-E-O:EP-PDI device is plotted as a function of continuous photoexcitation intensity, I_{exc}, at the wavelength of 532 nm. The dependence is of the form: $I_{sc} \propto (I_{exc})^{\alpha}$ with a slope $\alpha = 0.93$. For comparison, noninverted PBDTTT-E-O:EP-PDI devices,

Table 2. Main Solar Cell Parameters of Noninverted Devices with Photoactive Layers Annealed at Different Annealing Temperatures and of the Inverted Device (i-OPV) with Photoactive Layer Annealed at 100 °C[a]

device	V_{oc} (V)	J_{sc} (mA cm^{-2})	FF (%)	best PCE (%)	averaged PCE (%)
as spun	0.490 ± 0.008	2.80 ± 0.11	31.9 ± 0.7	0.50	0.47 ± 0.02
40 °C	0.540 ± 0.014	3.12 ± 0.08	34.6 ± 0.3	0.63	0.67 ± 0.04
80 °C	0.530 ± 0.010	3.29 ± 0.05	34.5 ± 1.2	0.69	0.65 ± 0.04
100 °C	0.600 ± 0.005	4.49 ± 0.13	47.2 ± 0.9	1.43	1.37 ± 0.06
120 °C	0.590 ± 0.004	4.32 ± 0.16	48.7 ± 0.7	1.38	1.34 ± 0.04
160 °C	0.630 ± 0.004	4.19 ± 0.05	44.8 ± 1.0	1.31	1.28 ± 0.03
200 °C	0.620 ± 0.011	3.62 ± 0.10	41.2 ± 0.6	1.03	0.99 ± 0.03
i-OPV, 100 °C	0.670 ± 0.004	4.80 ± 0.06	46.1 ± 1.1	1.90	1.81 ± 0.09

[a]The noninverted devices were characterized under 0.93 Sun (AM1.5G), whereas the inverted devices (i-OPV) where characterized under 0.83 Sun (AM1.5G).

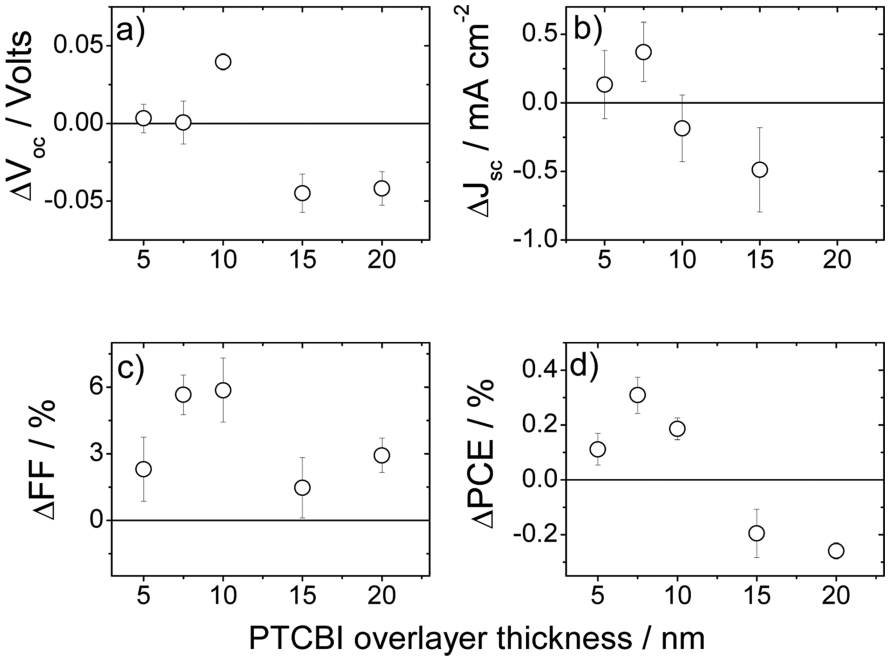

Figure 8. Observed difference in the main device metrics between solar cells of PBDTTT-E-O:EP-PDI devices with and without a thin PTCBI overlayer of variable overlayer thickness: (a) difference in the open-circuit voltage $\Delta V_{oc} = V_{oc}(\text{PTCBI}) - V_{oc}$, (b) difference in the short-circuit current $\Delta J_{sc} = J_{sc}(\text{PTCBI}) - J_{sc}$, (c) difference in the fill factor ΔFF = FF(PTCBI) − FF, and (d) difference in the power conversion efficiency ΔPCE = PCE(PTCBI) − PCE (see text).

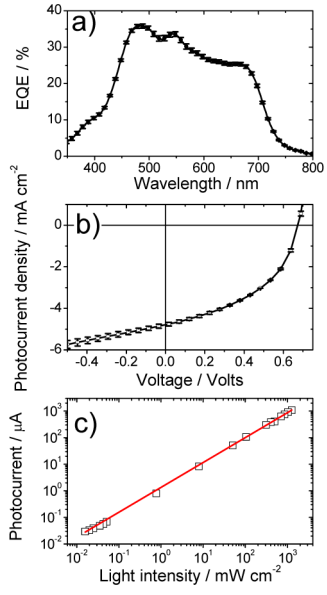

Figure 9. (a) External quantum efficiency (% EQE), (b) *J*−*V* curves, and (c) light intensity dependence of the device photocurrent (steady state photoexcitation at 532 nm) of an inverted OPV device with a photoactive layer of PBDTTT-E-O:EP-PDI 30:70 wt %, annealed at 100 °C after metal anode deposition. The device geometry was glass/ITO/ZnO/PBDTTT-E-O:EP-PDI/V_2O_5/Ag. Both EQE and *J*−*V* data are obtained as the average of five devices.

annealed at 100 °C after the deposition of Al electron-collecting electrodes, exhibited slopes of $\alpha = 0.9$ and $\alpha = 0.48$, for light intensity values between 0.1−15 mW/cm^2 and 15−1200 mW/cm^2, respectively. The replacement of Al with Ca/Al exhibited slopes of $\alpha = 1$ and $\alpha = 0.74$, for light intensity values between 0.1−15 mW/cm^2 and 15−1200 mW/cm^2, respectively (see Figure S5 in the Supporting Information).

Charge Transport Properties. We evaluated the impact of structural order on the charge transport properties of PBDTTT-E-O:EP-PDI films. We have performed charge transport measurements in unipolar PBDTTT-E-O:EP-PDI devices (Supporting Information Figure S6). We have deduced the zero-field electron and hole mobilities for a range of thermal annealing temperatures based on the Mott−Gurney equation, by taking into account the Poole−Frenkel effect.[51] Hole mobilities were determined for devices where the PBDTTT-E-O:EP-PDI photoactive layer was sandwiched between glass/ITO/PEDOTT:PSS and Au electrodes (build-in voltage, V_{bi} = 0 V), whereas electron mobilities were determined for devices with glass/ITO/ZnO and Ca/Al electrodes (V_{bi} = 1.5 V). Earlier transport studies utilizing the space charge limited current model on a polymer similar to PBDTTT-E-O have reported a hole mobility value of 4×10^{-4} cm^2/V s.[41] The electron mobility for EP-PDI has been reported to be 3−8 × 10^{-4} cm^2/V s based on OFET devices.[52] For our systems, the extracted hole and electron mobility values are reported in Table 3 as a function of thermal annealing temperature.

Table 3. Room-Temperature Hole and Electron Zero-Field Mobility Values as a Function of Thermal Annealing Temperature for the PBDTTT-E-O:EP-PDI Photoactive Layer

temperature (°C)	μ_h (cm^2/V s)	μ_e (cm^2/V s)
as spun	$3.8 \times 10^{-6} \pm 3.5 \times 10^{-6}$	$0.1 \times 10^{-6} \pm 0.1 \times 10^{-6}$
40	$6.3 \times 10^{-6} \pm 3.7 \times 10^{-6}$	$0.2 \times 10^{-6} \pm 0.1 \times 10^{-6}$
80	$39.4 \times 10^{-6} \pm 8.3 \times 10^{-6}$	$0.6 \times 10^{-6} \pm 0.1 \times 10^{-6}$
100	$48.3 \times 10^{-6} \pm 11.7 \times 10^{-6}$	$7.5 \times 10^{-6} \pm 0.7 \times 10^{-6}$
120	$33.5 \times 10^{-6} \pm 3.5 \times 10^{-6}$	$3.2 \times 10^{-6} \pm 1.4 \times 10^{-6}$
160	$52.5 \times 10^{-6} \pm 4.8 \times 10^{-6}$	$1.8 \times 10^{-6} \pm 0.2 \times 10^{-6}$
200	$55.9 \times 10^{-6} \pm 17.7 \times 10^{-6}$	$1.1 \times 10^{-6} \pm 0.1 \times 10^{-6}$

Despite the high EP-PDI content in the PBDTTT-E-O:EP-PDI blend films, hole mobility is found to be higher than electron mobility at all studied annealing temperatures. The hole/electron mobility ratio reaches a value of six at the annealing temperature of 100 °C. We note that for the case of the electron-only devices the employed Mott−Gurney model was applicable only for the high voltage regime of the $J-V$ curves. Previous studies of electron transport in organic materials have also shown that the accurate reproduction of the dark $J-V$ curves is achieved only after considering a distribution of trap-level energies in the density of states where charge transport takes place.[53] The presence of traps in the PDI-based blend films most likely is related with the structural defects present in the multicrystalline PDI phase. The determination of the total density of traps and of the energy that characterizes the trap distribution in the EP-PDI domains is beyond the scope of this work.

4. DISCUSSION

On the basis of the energetics of the PBDTTT-E-O:EP-PDI blend both processes of photoinduced electron and hole transfer have a high driving force with values: ΔE_{LUMO} = 0.56 eV and ΔE_{HOMO} = 1.11 eV, for electron transfer and hole transfer, respectively. We have verified that the PL emission of PBDTTT-E-O in the blend was completely quenched at all thermal annealing temperatures studied, after selectively photoexciting the polymer. On the basis of the WAXS results, PBDTTT-E-O backbones form relatively small ordered stacks in the range 4.3−7.5 nm. This should correspond to the diffusion length of the PBDTTT-E-O excitons.

In the PBDTTT-E-O:EP-PDI blend film, the EP-PDI component exhibits a hierarchical self-assembly; EP-PDI monomers self-organize via $\pi-\pi$ stacking into columns, the length of which is limited by defects. The EP-PDI columns are then positioned in a lattice with lateral correlation length that defines the size of the smallest ordered EP-PDI domains. Thermal annealing is strongly affecting the *intra*columnar order by increasing intracolumnar correlations between EP-PDI disks. In contrast, EP-PDI *inter*columnar order is not significantly affected by thermal treatment. The WAXS results further revealed the absence of tilting of disks within the columns. It is also found that the majority of the EP-PDI component is very well organized even in the as-spun film. According to WAXS, ordered EP-PDI columns with intracolumnar length of 12 nm are already present in the as-spun PBDTTT-E-O:EP-PDI domains that can become as long as 19 nm following annealing at 180 °C. In combination with the spectral data of the UV−vis absorption and time-integrated PL we can suggest that the larger portion of the EP-PDI excitons converts efficiently to homo-CT states within the H-aggregates of the EP-PDI columns and results in the excimer-type PL of EP-PDI. The residue of the EP-PDI exciton population can diffuse in the defected areas of the EP-PDI columns that will be composed from weakly associated EP-PDI monomers. At this stage we cannot quantify the fraction of the exciton population that converts to homo-CT population. However, the high organization of the EP-PDI columns that is suggested by WAXS increases the probability for the dominance of the homo-CT states, especially after thermal annealing where improved intracolumnar correlation lengths are obtained. No PL signal of the EP-PDI exciton was detected in the PL spectra of the PBDTTT-E-O:EP-PDI blend films. Recent studies on aggregates of a similar PDI derivative in solution suggest that self-trapping of the EP-PDI exciton takes place in the femtosecond time scale.[46]

The energy transfer from EP-PDI excimer to the polymer is likely to operate based on a beyond-Forster mechanism.[54] Following the transfer it is expected that the activated PBDTTT-E-O excitons will efficiently charge transfer at the polymer/EP-PDI interfaces. The fraction of the EP-PDI excimers that will not energy transfer to PBDTTT-E-O can contribute to the generation photocurrent only if they dissociate at the EP-PDI/polymer interface. Therefore, the size of the EP-PDI domain will dictate the dissociation efficiency of the EP-PDI excimer. The diffusion length of the PDI homo-CT state is L_{homoCT} = 10 ± 5 nm,[37] that is, comparable to the intracolumnar correlation length found in the unannealed and annealed PBDTTT-E-O:EP-PDI films up to 120 °C. Indeed the quenching of the EP-PDI excimer luminescence is close to unity for the case where the intracolumnar correlation length is comparable to the homo-CT diffusion length. This confirms that EP-PDI homo-CT states can diffuse toward the EP-PDI/polymer interface and contribute to the generation of photocurrent. The reduced quenching of the EP-PDI excimer luminescence at 620 nm observed with increasing annealing temperature is attributed to the diffusion-limited arrival at the homo-CT states at EP-PDI/polymer interface. It is found that with annealing the EP-PDI PL quenching efficiency reduces by 15% (Table S2 in Supporting Information) when the EP-PDI intracolumnar correlation length increases by 40% (Table 1).

Apart from matching the size of the EP-PDI column length with the diffusion length of the EP-PDI homo-CT state, the dissociation of the excimer states requires favorable energetics that will provide the necessary driving force for passing the energetic barrier of excimer binding energy. The energy of the unbound charge-separated (CS) state for the PBDTTT-E-O:EP-PDI system corresponds to E_{CS} = |$HOMO_{polymer}$| − |$LUMO_{PDI}$| = 1.21 eV. This is a difference of $\Delta E_{ton\text{-}CS}$ = 1.12 eV lower than the EP-PDI singlet exciton energy, E_{ton} (PL maximum at 2.33 eV[35]), and $\Delta E_{mer\text{-}CS}$ = 0.79 eV lower than the PDI excimer energy, E_{mer} (PL maximum at 2.00 eV). In respect to the exciton state, the PDI excimer is stabilized by 0.33 eV, as evidenced by the spectral red-shift in the excimer luminescence.[30] In a simplified picture, the excimer binding energy, $E_{b,mer}$, can be considered as the sum of excimer stabilization energy, E_{stab}, and the EP-PDI exciton binding energy $E_{b,ton}$. Therefore, excimer dissociation can take place at the EP-PDI/polymer interface when the difference between the energy of the PDI homo-CT state and the CS state is greater than or equal to the sum of the PDI exciton binding energy and PDI excimer stabilization energy; that is, $E_{b,ton} + E_{stab} \leq E_{mer} - E_{CS}$.

We note that the triplet energy level of PDI is at E_T = 1.2 eV,[55,56] i.e., comparable to the energy of the CS state of the PBDTTT-E-O:EP-PDI blend system. The relatively high photocurrent generation efficiency of the system suggests that in their majority the homo-CT states of EP-PDI do not convert to triplet states.[57] Instead they can energy transfer to the polymer phase or they can reach the EP-PDI/polymer heterojunction where they can dissociate. Hence, the activation of the excimer state of PDI is useful in preventing the funneling of singlet PDI excitons to the triplet PDI manifolds. The upper limit for the formation time of the homo-CT state of PDI is 100 ps,[31,46] and therefore the intersystem crossing rate k_{ISC} must be lower than $k_{ISC} < 10^{10}$ s^{-1}. Figure 10 illustrates the energetics of the PDI excited states and visualizes the photophysical

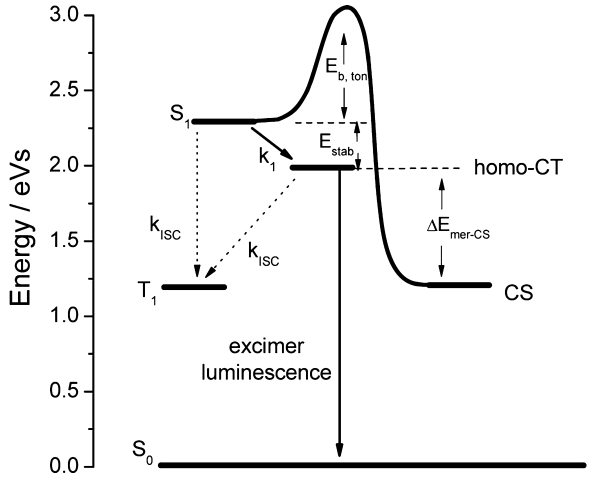

Figure 10. Energy level diagram of the PDI excited states that can participate in the generation of free charges in a PDI/polymer blend film after the photoexcitation of PDI. The singlet and triplet PDI exciton energies correspond to S_1 and T_1, respectively, whereas the energy of the free charges corresponds to the charge-separated (CS) state. The PDI singlet exciton can be stabilized by E_{stab} to the homo-CT state of PDI with a conversion rate of k_1. Alternatively, a singlet exciton can undergo intersystem crossing with a rate k_{ISC}. Once the homo-CT state of PDI is formed, it can (i) undergo intersystem crossing to the T_1 state,[33] (ii) return to the ground state (S_0) by emitting a photon with an energy of E_{mer} that corresponds to the excimer luminescence, and (iii) dissociate at the PDI/polymer interface for generating the CS state. The latter process is possible when the condition $E_{b,ton} + E_{stab} \leq E_{mer} - E_{CS}$ is met.

processes involved in charge photogeneration by adapting a particle-in-a-box picture. The description of excimer dissociation with the use of molecular orbitals could be enabled in light of computational data such as nonadiabatic quantum mechanics/molecular mechanics simulations.[38]

We now discuss the relationship between the charge mobility and the microstructure of the PDI network in the blend films. With respect to photocurrent generation another (larger) length scale plays also a role. Larger bicontinuous networks (aggregates) can serve as percolation pathways for the transport of the mobile charges to the device electrodes. FOM and AFM images clearly show that elongated features with sharp boundaries, 150 nm width and few hundred nanometer length, start to appear following thermal annealing above 40 °C. The structural motifs of the blend components in the nanoscopic length scale are directly affecting the process of charge transport. According to the WAXS results, order in the majority component of the blend, i.e., within the EP-PDI columns, is greatly improving with thermal annealing. Thermal treatment has no influence on the intercolumnar coherence length of the EP-PDI domains, but it helps in the formation of mesoscopic EP-PDI crystalline aggregates. For the minor component of the blend, i.e., the PBDTTT-E-O, the improvement in the structural order is not as pronounced as for EP-PDI. The deduced carrier mobility for electrons and holes further confirms that charge transport improves with thermal annealing. However, thermal annealing has a quantitatively different effect on hole and electron transport. In comparison to the as-spun case, hole transport in the layer annealed at 100 °C increases by an order of magnitude, but electron transport improves by almost 2 orders of magnitude. More importantly, electron mobility is reduced for annealing temperatures higher than 100 °C, but hole mobility is not greatly affected. The observed increase in hole mobility is attributed to the increased number of well-organized polymer backbones in the polymer domain that is induced by the heating treatment. Despite the stronger dependence of electron mobility on thermal annealing, hole mobility remains six times higher than electron mobility, for the optimum annealing temperature of 100 °C.

Generally in polymers electron mobility is known to be inferior to hole mobility due to the presence of charge traps within the material energy bandgap.[58] For the case of the PBDTTT-E-O:EP-PDI blend the main reason for low electron mobility is related to the improper connectivity of the EP-PDI domains. Electron transport takes place mainly within the EP-PDI columns of adjacent EP-PDI domains that are not always aligned suitably for achieving an efficient electronic coupling. The connectivity of these domains is therefore achieved by the small fraction of the weakly associated EP-PDI monomers that are present between the adjacent ordered EP-PDI domains. The macroscopic electron mobility of the blend is dictated by the effective connectivity of the EP-PDI columns in the photoactive layer. Thermal annealing at temperatures higher than 100 °C results in the formation of well-ordered EP-PDI columns that can conduct charge efficiently within the EP-PDI domain, but they are disconnected from the adjacent domains. This is the result of the increased order in the EP-PDI phase that has a negative effect on the macroscopic electron transport. The reduction in electron mobility for annealing at temperatures higher than 100 °C confirms the positive role of the weakly associated EP-PDI monomers in electron transport. The reduction in the fraction of disordered EP-PDI is responsible for the poor connectivity of the ordered EP-PDI domains. Previous results on EP-PDI blend with poly(fluorene) copolymers suggested the requirement for balanced features of order and disorder in EP-PDI phases made of EP-PDI aggregates. The efficient macroscopic transport of the photogenerated electrons was shown to take place along layers of EP-PDI aggregates that were horizontally placed in respect to the device substrate and that were vertically interconnected by disordered displacements of the EP-PDI aggregates in each layer.[35] Other studies on films of PDI-based organosilane uniaxially aligned columnar aggregates have also reported that the electrical conductivity along adjacent PDI columnar aggregates can be enhanced if a partial overlap between PDI disks of the adjacent columns is achieved. Nonimpeded electron hopping along the columns leads to conductivity values as high as 2.2×10^{-2} S/cm in the direction vertical to the long axis of the disordered PDI columnar aggregates.[59] Additional evidence on the positive effects of disorder on the process of charge transport and photocurrent generation in PDI-based OPVs was provided recently with the realization of efficient OPV devices based on disordered PDI dimers.[25,40] These findings are in agreement with theoretical studies suggesting that the intercolumnar propagation of charge carriers in PDIs can be supported by the dynamically induced electronic coupling of adjacent PDI columns.[60]

The poor connectivity of the EP-PDI columns that impedes electron transport inevitably leads to the recombination of the mobile charges. This is an additional factor that limits the power conversion efficiency of the PBDTTT-E-O:EP-PDI devices. Our measurements cannot provide direct information on the type of recombination that takes place in the PDI-based blend films we studied. Transient absorption spectroscopy in blend films[61] and transient optoelectronic measurements in

OPV devices[62] are expected to provide quantitative information on the charge recombination loss channels that dominate in the PBDTTT-E-O:EP-PDI system. Both types of geminate[63] and nongeminate[31] charge recombination have been suggested for different PDI-based blend films. In agreement with previously studied PDI-based polymeric OPV systems,[31] the noninverted device geometry of the PBDTTT-E-O:EP-PDI system bearing the Al-based electron-collecting electrode exhibited a light intensity dependent J_{sc} with a power law exponent of $\alpha = 0.48$. This implies that a fraction of the photogenerated charges is lost due to bimolecular recombination. However, the same PBDTTT-E-O:EP-PDI device geometry exhibited a power law exponent of $\alpha = 0.74$ when the Ca-based electron-collecting electrode was used. This value of the power exponent indicates the build-up of space charge.[64,65] In both types of noninverted devices, the hole/electron mobility ratio remains unchanged and lower than an order of magnitude. Therefore, it is very likely that the dependence of J_{sc} of PDI-based OPV devices on photoexcitation intensity is significantly affected by the nature of the metal electrode that is used as the electron-collecting contact. Previous reports have indicated that PDI derivatives and their analogues can be reactive with metal contacts such as Al-based electrodes.[42,66] Upon inverting the device geometry, the linearity of the short-circuit device photocurrent on photoexcitation intensity was recovered (Figure 9c). In terms of PCE efficiency the i-OPV device reached a PCE = 1.9%, that is, more than 21 times higher than that previously received by devices with photoactive layers of EP-PDI mixed with the fluorene copolymer poly(9,9′-dioctylfluorene-co-benzothiadiazole).[35] The improvement suggests that the PDI component of the PBDTTT-E-O:EP-PDI blend system segregates on the bottom section of the film, away from the layer/air interface. The PDI enrichment of the bottom sections of the PBDTTT-E-O:EP-PDI layer could originate by the different type of substrate that is utilized in the i-OPV geometry, presumably due to the different surface energy of PEDOT:PSS and ZnO layers. The topic of vertical phase separation in PDI-based OPV blends will be discussed in a separate communication.

Additional information on the properties of the interface between the blend surface and the electron-collecting electrode is provided by the devices with the PTCBI overlayer. The electrical characterization of PBDTTT-E-O:EP-PDI solar cells with photoactive layers annealed before (preannealed device) and after (postannealed device) the metal cathode deposition (Table S1 in Supporting Information) was performed. In respect to the as-spun device we found that the J_{sc} of the preannealed device dropped by five times, whereas the J_{sc} of the postannealed device improved by 1.5 times. Therefore, although the formation of mesoscopic EP-PDI aggregates improves device photocurrent, it does not necessarily maximize the extraction of the photogenerated free electrons due to the rough surface of the photoactive layer caused by the EP-PDI rods. For layers annealed at the optimum temperature of 100 °C, high-resolution AFM imaging (500 nm scan length) finds a surface roughness of 4.80 nm. For postannealed devices the device performance improves substantially. Most likely the improvement is due to the elimination of defected interface sites that are caused by voids at the layer/electrode interface when the layer surface is rough.[67] In the preannealed device, this highly rough surface leads to poor charge collection and low photocurrent generation. A lower concentration of defect sites is expected in the postannealed device. High-resolution cross-sectional scanning electron microscopy imaging could elucidate this point. At present, in line to our suggestion is the fact that the deposition of the smooth PTCBI overlayer reduces the surface roughness of the bilayer down to 1.77 nm, and it increases both parameters of FF and J_{sc} of the device, leading the delivery of a power conversion efficiency of 1.68% ± 0.06%. Since PTCBI and EP-PDI are very similar PDI derivatives we assign the beneficial effect of the PTCBI overlayer to the achieved surface passivation rather to an improved selectivity of the electrode contact[68−70] toward the PTCBI component.

5. CONCLUSIONS

We have studied the structure−function relationships in the efficient OPV blend of PBDTTT-E-O:EP-PDI. The selection of the low-energy gap PBDTTT-E-O donor extends the absorption profile of the blend towards the lower photon energies of the visible spectrum, and it results in high photocurrent generation efficiency. We addressed the correlation between the local (columnar) and global (aggregate) structure of the PBDTTT-E-O:EP-PDI system with the electrical properties of the corresponding OPV devices. The local structure of the blend revealed a hierarchical self-assembly of the EP-PDI mesophase in the blend as verified by WAXS. The structural results are in agreement with the spectroscopic data of UV−vis and PL spectra that verify the formation of H-aggregates and the activation of homo-CT EP-PDI species that exhibit an excimer-like luminescence.

Our results demonstrate the necessity for accurately engineering the aggregation of EP-PDI in the OPV layer. The presence of disordered EP-PDI aggregates is essential both for the efficient dissociation of the EP-PDI excimers at the EP-PDI/polymer interface and for the optimum charge transport properties of the OPV layer. We provide rational guidelines for optimizing the microstructure of PDI-based excimeric OPV layers; the PDI columnar length must be kept comparable to the diffusion length of the PDI homo-CT states. Once these states arrive at the PDI/polymer heterojunction, excimer dissociation can take place if the energetics of the blend can provide a sufficient driving force that will surmount the excimer binding energy. The stabilization energy of the PDI excimers must be as low as possible so that the difference between exciton and excimer binding energy is minimal. Low excimer stabilization energy is plausible for PDI aggregates that exhibit weak intermolecular coupling between their PDI monomers. Some disorder within the PDI columns is, at the same time, necessary for the efficient electronic coupling of adjacent PDI columns that facilitates intercolumnar electron transport and provides the percolation path for the electrons to the device contacts. The precise molecular engineering of the PDI scaffold is expected to maximize the efficiency of charge photogeneration and transport processes in PDI-based excimeric solar cells. In addition, the quality of interface between the top carrier-collecting electrode and the photoactive layer critically affects the efficiency of charge collection. The use of i-OPV device geometries is recommended for the efficient performance of PDI-based OPV devices.

■ ASSOCIATED CONTENT

Supporting Information

Atomic force microscopy images, photophysical data on the spectral overlap of the EP-PDI excimer luminescence and the PBDTTT-E-O absorption, thermal-annealing-dependent quenching efficiency of the EP-PDI luminescence, photoexcitation-intensity-dependent short-circuit photocurrent for

PBDTTT-E-O:EP-PDI devices with different electron-collecting electrodes, space-charge-limited-current data of unipolar PBDTTT-E-O:EP-PDI devices, and thickness determination of the PBDTTT-E-O:EP-PDI and PS:PDI layers. This material is available free of charge via the Internet at http://pubs.acs.org.

AUTHOR INFORMATION

Corresponding Author

*E-mail: pekeivan@iit.it.

Author Contributions

The manuscript was written through contributions of all authors. All authors have given approval to the final version of the manuscript.

Notes

The authors declare no competing financial interest.

ACKNOWLEDGMENTS

Funding provided by FP7-PEOPLE-2011-IEF. PEK acknowledges the financial support of an Intra European Marie Curie Fellowship (project DELUMOPV) and thanks Daniele Fazzi for useful discussions.

REFERENCES

(1) Thompson, B. C.; Fréchet, J. M. J. *Angew. Chem., Int. Ed.* **2008**, *47*, 58−77.
(2) Sondergaard, R. R.; Hosel, M.; Krebs, F. C. *J. Polym. Sci., Part B: Polym. Phys.* **2013**, *51*, 16−34.
(3) Sariciftci, N. S.; Smilowitz, L.; Heeger, A. J.; Wudl, F. *Science* **1992**, *258*, 1474.
(4) Halls, J. J. M.; Walsh, C. A.; Greenham, N. C.; Marseglia, E. A.; Friend, R. H.; Moratti, S. C.; Holmes, A. B. *Nature* **1995**, *376*, 498.
(5) Clarke, T. M.; Durrant, J. R. *Chem. Rev.* **2010**, *110*, 6736−6767.
(6) Li, G.; Zhu, R.; Yang, Y. *Nat. Photonics* **2012**, *6*, 153−161.
(7) He, Z.; Zhong, C.; Su, S.; Xu, M.; Wu, H.; Cao, Y. *Nat. Photonics* **2012**, *6*, 591−595.
(8) Azzopardi, B.; Emmott, C. J. M.; Urbina, A.; Krebs, F. C.; Mutale, J.; Nelson, J. *Energy Environ. Sci.* **2011**, *4*, 3741−3753.
(9) Anthony, J. E. *Chem. Mater.* **2011**, *23*, 583−590.
(10) Chochos, C. L.; Tagmatarchis, N.; Gregoriou, V. *RSC Adv.* **2013**, *3*, 7160−7181.
(11) Sonar, P.; Pui Fong Lim, J.; Leok Chan, K. *Energy Environ. Sci.* **2011**, *4*, 1558−1574.
(12) Zhao, X.; Zhan, X. *Chem. Soc. Rev.* **2011**, *40*, 3728−3743.
(13) Lin, Y.; Li, Y.; Zhan, X. *Chem. Soc. Rev.* **2012**, *41*, 4245−4272.
(14) Kamm, V.; Battagliarin, G.; Howard, I. A.; Pisula, W.; Mavrinskiy, A.; Li, C.; Müllen, K.; Laquai, F. *Adv. Energy Mater.* **2011**, *1*, 297−302.
(15) Schmidt-Mende, L.; Fechtenkoetter, A.; Müllen, K.; Moons, E.; Friend, R. H.; MacKenzie, J. D. *Science* **2001**, *293*, 1119−1122.
(16) Li, J.; Dierschke, F.; Wu, J.; Grimsdale, A. C.; Müllen, K. *J. Mater. Chem.* **2006**, *16*, 96−100.
(17) Shoaee, S.; Clarke, T. M.; Huang, C.; Barlow, S.; Marder, S. R.; Heeney, M.; McCulloch, I.; Durrant, J. R. *J. Am. Chem. Soc.* **2010**, *132*, 12919−12926.
(18) Li, C.; Wonneberger, H. *Adv. Mater. (Weinheim, Ger.)* **2012**, *24*, 613−636.
(19) Zhan, X.; Facchetti, A.; Barlow, S.; Marks, T. J.; Ratner, M. A.; R., W. M.; Marder, S. R. *Adv. Mater. (Weinheim, Ger.)* **2011**, *23*, 268−284.
(20) Sharenko, A.; Proctor, C. M.; van der Poll, T. S.; Henson, Z. B.; Nguyen, T.-Q.; Bazan, G. C. *Adv. Mater. (Weinheim, Ger.)* **2013**, *25*, 4403−4406.
(21) Zhan, X.; Tan, Z.; Domercq, B.; An, Z.; Zhang, X.; Barlow, S.; Li, Y.; Zhu, D.; Kippelen, B.; Marder, S. R. *J. Am. Chem. Soc.* **2007**, *129*, 7246−7247.
(22) Tan, Z.; Zhou, E.; Zhan, X.; Wang, X.; Li, Y.; Barlow, S.; Marder, S. R. *Appl. Phys. Lett.* **2008**, *93*, 073309/1−073309/3.
(23) Struijk, C. W.; Sieval, A. B.; Dakhorst, J. E. J.; van Dijk, M.; Kimkes, P.; Koehorst, R. B. M.; Donker, H.; Schaafsma, T. J.; Picken, S. J.; van de Craats, A. M.; Warman, J. M.; Zuilhof, H.; Sudhölter, E. J. R. *J. Am. Chem. Soc.* **2000**, *122*, 11057−11066.
(24) Bu, L.; Guo, X.; Yu, B.; Qu, Y.; Xie, Z.; Yan, D.; Geng, Y.; Wang, F. *J. Am. Chem. Soc.* **2009**, *131*, 13242−13243.
(25) Rajaram, S.; Shivanna, R.; Kandappa, S. K.; Narayan, K. S. *J. Phys. Chem. Lett.* **2012**, *3*, 2405−2408.
(26) Liu, S.-G.; Sui, G.; Cormier, R. A.; Leblanc, R. M.; Gregg, B. A. *J. Phys. Chem. B* **2002**, *106*, 1307.
(27) Chen, Z.; Stepanenko, V.; Dehm, V.; Prins, P.; Siebbeles, L. D. A.; Seibt, J.; Marquetand, P.; Engel, V.; Wurthner, F. *Chem.−Eur. J.* **2007**, *13*, 436.
(28) Ferguson, A. J.; Jones, T. S. *Chem. Phys. Lett.* **2009**, *474*, 137−140.
(29) Yi, Y.; Coropceanu, V.; Bredas, J.-L. *J. Mater. Chem.* **2011**, *21*, 1479−1486.
(30) Dittmer, J. J.; Marseglia, E. A.; Friend, R. H. *Adv. Mater. (Weinheim, Ger.)* **2000**, *12*, 1270.
(31) Howard, I. A.; Laquai, F.; Keivanidis, P. E.; Friend, R. H.; Greenham, N. C. *J. Phys. Chem. C* **2009**, *113*, 21225.
(32) Fink, R. F.; Seibt, J.; Engel, V.; Renz, M.; Kaupp, M. L., S.; Zhao, H.-M.; Pfister, J.; Wurthner, F.; Engels, B. *J. Am. Chem. Soc.* **2008**, *130*, 12858−12859.
(33) Veldman, D.; Chopin, S. M. A.; Meskers, S. C. J.; Janssen, R. A. J. *J. Phys. Chem. A* **2008**, *112*, 8617−8632.
(34) Birks, J. B. *Rep. Prog. Phys.* **1975**, *38*, 903.
(35) Keivanidis, P. E.; Howard, I. A.; Friend, R. H. *Adv. Funct. Mater.* **2008**, *18*, 3189−3202.
(36) Veldman, D.; Chopin, S. M. A.; Meskers, S. C. J.; Groeneveld, M. M.; Williams, R. M.; Janssen, R. A. J. *J. Phys. Chem. A* **2008**, *112*, 5846−5857.
(37) Vertsimakha, Y.; Lutsyk, P.; Palewska, K.; Sworakowski, J.; Lytvyn, O. *Thin Solid Films* **2007**, *515*, 7950−7957.
(38) Jailaubekov, A. E.; Willard, A. P.; Tritsch, J. R.; Chan, W.-L.; Sai, N.; Gearba, R.; Kaake, L. G.; Williams, K. J.; Leung, K.; Rossky, P. J.; Zhu, X.-Y. *Nat. Mater.* **2013**, *12*, 66−73.
(39) Katoh, R.; Sinha, S.; Murata, S.; Tachiya, M. *J. Photochem. Photobiol., A* **2001**, *145*, 23−30.
(40) Zhang, X.; Lu, Z.; Ye, L.; Zhan, C.; Hou, J.; Zhang, S.; Jiang, B.; Zhao, Y.; Huang, J.; Zhang, S.; Liu, Y.; Shi, Q.; Liu, Y.; Yao, J. *Adv. Mater. (Weinheim, Ger.)* **2013**, DOI: 10.1002/adma.201300897.
(41) Chen, H.-Y.; Hou, J.; Zhang, S.; Liang, Y.; Yang, G.; Yang, Y.; Yu, L.; Wu, Y.; Li, G. *Nat. Photonics* **2009**, *3*, 649−653.
(42) Keivanidis, P. E.; Laquai, F.; Howard, I. A.; Friend, R. H. *Adv. Funct. Mater.* **2011**, *21*, 1355−1363.
(43) Sun, Y.; Seo, J.-H.; Takacs, C. J.; Seifter, J.; Heeger, A. J. *Adv. Mater. (Weinheim, Ger.)* **2011**, *23*, 1679−1683.
(44) Erten, S.; Meghdadi, F.; Gunes, S.; Koeppe, R.; Sariciftci, N. S.; Icli, S. *Eur. Phys. J. Appl. Phys.* **2007**, *36*, 225.
(45) Ferguson, A. J.; Jones, T. S. *J. Phys. Chem. B* **2006**, *110*, 6891−6898.
(46) Schubert, A.; Settels, V.; Liu, W.; Würthner, F.; Meier, C.; Fink, R. F.; Schindlbeck, S.; Lochbrunner, S.; Engels, B.; Engel, V. *J. Phys. Lett.* **2013**, *4*, 792−796.
(47) Tasios, N.; Grigoriadis, C.; Hansen, M. R.; Wonneberger, H.; Li, C.; Spiess, H. W.; Müllen, K.; Floudas, G. *J. Am. Chem. Soc.* **2010**, *132*, 7478.
(48) Veldman, D.; Ipek, O.; Meskers, S. C. J.; Sweelssen, J.; Koetse, M. M.; Veenstra, S. C.; Kroon, J. M.; van Bavel, S. S.; Loos, J.; Janssen, R. A. J. *J. Am. Chem. Soc.* **2008**, *130*, 7221.
(49) Keivanidis, P. E.; Clarke, T. M.; Lilliu, S.; Agostinelli, T.; Macdonald, J. E.; Durrant, J. R.; Bradley, D. D. C.; Nelson, J. *J. Phys. Chem. Lett.* **2010**, *1*, 734−738.
(50) Tang, C. W. *Appl. Phys. Lett.* **1986**, *48*, 183.
(51) Machui, F.; Rathgeber, S.; Li, N.; Ameri, T.; Brabec, C. J. *J. Mater. Chem.* **2012**, *22*, 15570−15577.

(52) Singh, T. B.; Erten, S.; Günes, S.; Zafer, C.; Turkmen, G.; Kuban, B.; Teoman, Y.; Sariciftci, N. S.; Icli, S. *Org. Electron.* **2006**, *7*, 480−489.
(53) Blom, P. W. M.; de Jong, M. J. M.; Vleggaar, J. J. M. *Appl. Phys. Lett.* **1996**, *68*, 3308−3310.
(54) Scholes, G. D. *Int. Rev. Phys. Chem.* **2011**, *30*, 49−77.
(55) Ford, W. E.; Kamat, P. V. *J. Phys. Chem.* **1987**, *91*, 6373−6380.
(56) Castellano, F. N.; Goeb, S.; Rachford, A. A. *J. Am. Chem. Soc.* **2008**, *130*, 2766.
(57) Veldman, D.; Meskers, S. C. J.; Janssen, R. A. J. *Adv. Funct. Mater.* **2009**, *19*, 1939−1948.
(58) Nicolai, H. T.; Kuik, M.; Wezelaer, G. A. H.; de Boer, B.; Campbell, C.; Risko, C.; Bredas, J.-L.; Blom, P. W. M. *Nat. Mater.* **2012**, *11*, 882−887.
(59) Mizoshita, N.; Tani, T.; Inagaki, S. *Adv. Funct. Mater.* **2011**, *21*, 3291−3296.
(60) Di Donato, E.; Fornari, R. P.; Di Motta, S.; Li, Y.; Wang, Z.; Negri, F. *J. Phys. Chem. B* **2010**, *114*, 5327−5334.
(61) Etzold, F.; Howard, I. A.; Mauer, R.; Meister, M.; Kim, T.-D.; Lee, K.-S.; Baek, N. S.; Laquai, F. *J. Am. Chem. Soc.* **2011**, *133*, 9469−9479.
(62) Hawks, S. A.; Deledalle, F.; Yao, J.; Rebois, D. G.; Li, G.; Nelson, J.; Yang, Y.; Kirchartz, T.; Durrant, J. R. *Adv. Funct. Mater.* **2013**, *3*, 1201−1209.
(63) Shoaee, S.; An, Z.; Zhang, X.; Barlow, S.; Marder, S. R.; Duffy, W.; Heeney, M.; McCullochac, I.; Durrant, J. R. *Chem. Commun.* **2009**, 5445−5447.
(64) Mihailetchi, V. D.; Wilderman, J.; Blom, P. W. M. *Phys. Rev. Lett.* **2005**, *94*, 126602.
(65) Mihailetchi, V. D.; Xie, H.; de Boer, B.; Koster, L. J.; Blom, P. W. M. *Adv. Funct. Mater.* **2006**, *16*, 699−708.
(66) Heggie, D. A.; MacDonald, B. L.; Hill, I. G. *J. Appl. Phys.* **2006**, *100*, 104505.
(67) Gupta, D.; Mukhopadhyay, S.; Narayan, K. S. *Sol. Energy Mater. Sol. Cells* **2010**, *94*, 1309−1313.
(68) Steim, R.; R. K., F.; Brabec, C. J. *J. Mater. Chem.* **2010**, *20*, 2499−2512.
(69) Chen, L.-M.; Xu, Z.; Hong, Z.; Yang, Y. *J. Mater. Chem.* **2010**, *20*, 2575−2598.
(70) Ratcliff, E. L.; Zacher, B.; Armstrong, N. R. *J. Phys. Chem. Lett.* **2011**, *2*, 1337−1350.